Research Article | Vol. 27, No. 3 | 4 Feb 2019 | OPTICS EXPRESS 2886
Optics EXPRESS

Continuous-wave laser-induced welding and giant photoluminescence enhancement of Au nanospheres

CHENGBING QIN,[1,2,3] XIAORONG ZHANG,[1,2] WENJUN HE,[1,2] GUOFENG ZHANG,[1,2] RUIYUN CHEN,[1,2] YAN GAO,[1,2] LIANTUAN XIAO,[1,2,4] AND SUOTANG JIA[1,2]

[1]*State Key Laboratory of Quantum Optics and Quantum Optics Devices, Institute of Laser Spectroscopy, Shanxi University, Taiyuan, Shanxi 030006, China*
[2]*Collaborative Innovation Center of Extreme Optics, Shanxi University, Taiyuan, Shanxi 030006, China*
[3]*chbqin@sxu.edu.cn*
[4]*xlt@sxu.edu.cn*

Abstract: Photoluminescence (PL) of Au nanoparticles is appealing for various biological applications, owing to their unique advantages. However, widespread applications are still limited by their extremely low quantum yield. Here, we report on the giant PL enhancement of aggregated Au nanospheres by continuous-wave (CW) laser irradiation. Our studies show that the laser-induced PL enhancement is influenced by the wavelength and power density of irradiation laser, as well as the size of Au nanospheres. The averaged intensity of Au nanospheres after irradiation by 405 nm CW laser at power density of 6 MW/cm^2 is 75 times that of the as-prepared sample, where the highest enhancement of 150 folds is obtained. The giant PL enhancement is attributed to laser-induced photothermal welding and reshaping of adjacent Au nanospheres, which will dramatically enhance the incidence light field in the crevices around the welding areas by surface plasmon resonance. These studies not only declare that Au nanospheres are expected to find many new applications in PL-based biosensing and bioiamging, but also suggest that CW laser can be used as a versatile tool to weld and reshape the Au nanospheres in order to build up functionalized electronic and optoelectronic devices.

1. Introduction

Nobel metal nanoparticles, e.g., of Au and Ag, have attracted widespread interest over the past decades [1–3], in particular because of their promising applications ranging cross light harvesting [4], photocatalysis [5], sensing [6], and nonlinear optics [7]. These applications benefit from the collective oscillation of electrons on the nanoparticles surface that occurs when excited with light at an appropriate wavelength [8]. This phenomenon is known as surface plasmon resonance (SPR). SPR is sensitive to the morphology of Au nanoparticles [9], the surrounding dielectric media [10], as well as the interparticle plasmon coupling [11]. Amazingly, the local light field within the gap of coupled nanoparticles can be enhanced up to thousand-fold by the plasmon coupling [12]. The giant local field enhancement has been used to amplify the optical response of materials surrounding Au nanoparticles, including surface enhanced Raman scattering (SERS) [13], two-photon photoluminescence (TPPL) [14], second-harmonic generation [15], as well as metal-enhanced fluorescence [16].

Very recently, plasmon coupling has also been used to enhance photoluminescence (PL) of Au nanoparticles themselves. Development and enhancement of PL of Au nanoparticles is vital for biological applications, in view of their neither photoblinking nor photobleaching, as well as their nontoxicity and high biocompatibility [17,18]. Some efforts have focused on the PL enhancement of Au nanoparticles, where the enhancement on the TPPL of Au

#348370 https://doi.org/10.1364/OE.27.002886
Journal © 2019 Received 17 Oct 2018; revised 14 Dec 2018; accepted 25 Dec 2018; published 29 Jan 2019

Optics EXPRESS

nanospheres (NSs) by plasmon coupling at Xu group is most pronounced [19,20]. Using an oppositely charged polyelectrolyte, they determined enhancement factors of 25 folds for coupled 55-nm Au NSs [20]. And then, the huge enhancement up to 1.2×10^5 folds in TPPL was obtained for the linear trimer Au NSs [19]. Typically, the TPPL of Au NSs was excited by femtosecond laser in aqueous. In contrast, investigation and enhancement on single photon PL of Au NSs excited by conventional continuous wave (CW) laser rather than femtosecond laser are still challenge, in view of their extremely low quantum yield (ranging from 10^{-7} to 10^{-4} regarding with different sizes and shapes) [21–24]. However, these studies have greater practical significance, because CW lasers have been widely used in the Au NSs related biological applications, such as photothermal therapy and drug delivery [25–27]. In particular, they are more compact, inexpensive, portable and clinically compatible than pulsed laser [28].

Here, we report that PL of aggregated Au NSs can be dramatically enhanced by focused CW laser irradiation. A highest enhancement of 150 folds for 160-nm NSs is obtained after irradiation with 405 nm CW laser in several seconds at power density of 6 MW/cm^2. Systematic experimental results show that this laser-induced PL enhancement is sensitive to power density, laser wavelength, and their particle sizes. Scanning electron microscopy (SEM) reveals that adjacent Au NSs have been melted, welded and reshaped during laser irradiation. Thus, we propose that the dramatically enhanced local field around welded Au NSs results in giant PL enhancement. Our studies not only offer a route to enhance PL of Au NSs to develop their biological applications, but also provide an approach to weld noble metal nanostructures by commercial CW lasers to build up functionalized electronic and optoelectronic devices.

2. Experiment

2.1 Sample preparation

Cetyltrimethyl ammonium bromide (CATB) caped Au NSs, purchased from NanoSeedz Ltd. (Hong Kong SAR, China), were prepared by a seed-mediated growth approach modified from their previously reported works [29]. The marked diameters of three NSs used in the experiment are 160 nm (Product Code: NS-160-20), 100 nm (NS-100-20), and 60 nm (NS-60-20), respectively. For the sake of simplicity, these NSs are named as NS-160, NS-100, and NS-60 hereinafter for short, respectively. Samples used for laser irradiation were prepared by spin-coated the diluted solution (10^{-3} of the original solution) on the cleaned glass coverslip (Ted Pella).

2.2 Sample characterization

The absorption spectra of Au NSs were recorded by a Maya2000Pro Vis-NIR spectrometer (Ocean Optics, USA), which was also used to obtain PL spectra of NSs in solution. The morphology of NSs were characterized by SEM (SU8010, Hitachi, Japan) and transmission electron microscopy (TEM, Philips Model CM10, USA).

2.3 Optical setup

The experiments involved laser irradiation and PL imaging of Au NSs were performed with a home-built scanning confocal microscope. The experimental setup has been described elsewhere [30,31]. In particular, three lasers with the wavelength of 405 nm, 488 nm, and 532 nm in CW mode were used. They were not only acted as the excitation laser to take PL of Au NSs, but also used as the irradiation laser to enhance their PL. The laser power was in the region of 0.1 mW to 10 mW. The laser beam was tightly focused by a 100 × oil immersion objective lens with a high numerical aperture (NA = 1.3). The focused laser spot was about 200 nm in diameter, limited by diffraction. Thus, the power density was in the region of 0.3 MW/cm^2 to 30 MW/cm^2. The sample was placed on a piezo-electric translation nano-stage (PZT, Tritor, 200/20SG). PL from Au NSs was collected by the same objective. After passing

Optics EXPRESS

through a dichroic mirror (Semrock, Di01-R488-25x36), and a long-pass filter (Semrock, BLP01-496R-25) to block the back scattered laser as well as background signal, PL was further filtered spatially by a 100 μm pinhole and split by a beam splitter. Then one beam was detected by a single photon detector (PerkinElmer, SPCM-AQR-15), the other was transferred to a spectrometer to develop PL spectra. The transmission dark-field scattering spectroscopy of the aggregated Au NSs were performed on the same setup, by removal of the filters. The experiments were conducted by using a 100 W halogen lamp illumination through an air condenser and collecting the scattering light by the oil immersion objective.

3. Results and discussion

Au NSs with three different sizes were prepared to investigate laser-induced PL enhancement. To get the morphology and heterogeneity of these commercially available Au NSs, SEM and TEM were firstly used as the characterization, as shown in Fig. 1(a) and 1(b), respectively. Note that although the diameters of these NSs are similar, their actually sizes are quite different. Some of them even exhibit obvious tetrahedron or rod shape, as enlarged in Fig. 1(c). Figure 1(d) presents the size distribution of NS-160 drawn from its TEM characterizations. A broad distribution with the center of 152 nm and full width at half maximum (FWHM) of 26 nm can be clearly determined. Size distributions of other two kinds Au NSs (NS-100 and NS-60) are also determined (see Fig. 7 in Appendix). The relative broad distributions reveal the non-uniform and imperfect spherical shape of our Au NSs. Figure 1(e) presents the normalized extinction spectra of three different size NSs. Note that the dipolar plasmon mode redshifts gradually from 535 nm to 650 nm, as the averaged diameter increasing from 60 nm to 160 nm. For NS-160, quadrupolar plamon mode at 539 nm also appears. These phenomena agree well with previous reports [20,29]. Peak broadening is also clearly observed, which can be attributed to the increasing radiative losses for increased diameter of NSs. In contrast, no significant difference can be found in their PL spectra, as shown in Fig. 1(f). Furthermore, these PL spectra are closely resembles the corresponding scattering spectra (see Fig. 8 in Appendix). According to the suggestions from the previous investigations [32,33], we can attribute the PL of Au NSs to the spontaneous emission from the radiative recombination of hot carriers, where the enhanced spontaneous emission from the plasmonic mode results in the strong PL.

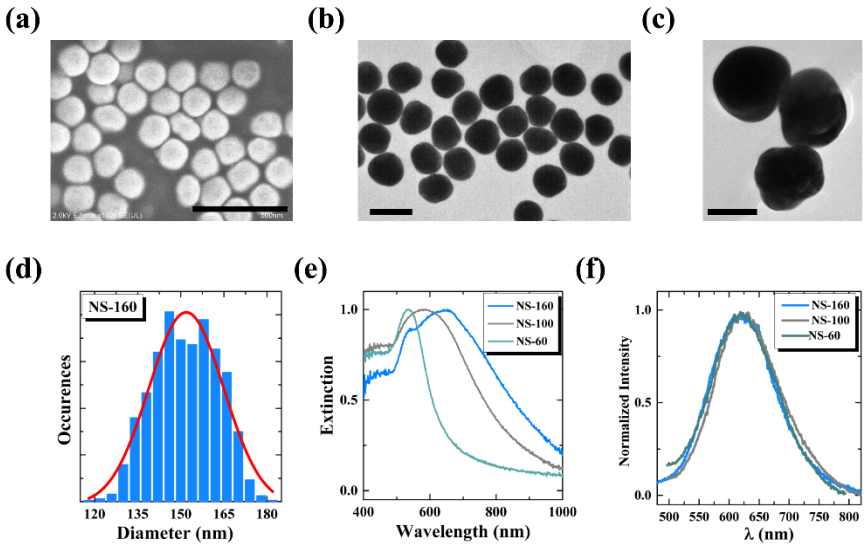

Fig. 1. (a) SEM and (b), (c) TEM images of Au nanospheres (NSs) with the averaged diameter of 160 nm (NS-160). Scale bar: (a) 500 nm; (b) 200 nm; (c) 100 nm. (d) Size distribution of

Optics EXPRESS

NS-160, fitted by Gauss function. (e) Normalized extinction and (f) photoluminescence (PL) spectra of three sizes Au NSs, respectively. PL spectra were excited by 405 nm CW laser.

Figure 2(a) presents typical confocal PL imaging of NS-160 spin-coated on the cleaned glass coverslip. Note that most areas exhibit similar patterns and intensities, indicating that the dispersion of Au NSs on the coverslip is reasonably good. However, some areas with much stronger PL can be easily observed, as the dashed circle highlighted in Fig. 2(a). These stronger PL are attributed to the emission of aggregated Au NSs, which can be proved by the SEM characterization of the prepared samples (Fig. 9 in Appendix). When focusing the laser on these areas with intensive power density, we found that their PL could be further enhanced, as shown in Fig. 2(b). Amazedly, a highest enhancement factor, *EF* (the enhanced PL divided by the initial value, PL_t/PL_0), of 150 folds has been determined in the experiment (Fig. 10 in Appendix). This implies that the quantum yield and PL intensity of Au NSs can be dramatically enhanced by CW laser irradiation. Further investigations show that PL trajectories for the enhanced areas present similar behavior, as shown in Fig. 2(b). In the beginning of laser irradiation, PL is relatively stable, as illustrated in the inset. Then, it will be enhanced sharply and hold the maximum intensity for a short duration. After a rapid decay from the maximum value, PL is quenching slowly and tends to be stable at last. To deeply gain insight into the enhancement mechanism, PL spectra of Au NSs during laser irradiation were collected synchronously, as shown in Fig. 2(c). It can be found that not only the intensities are enhanced dramatically, but also the spectral profiles are varied obviously. Redshift of the peak positions can be clearly determined, as highlighted by the dotted line. Similar variations of scattering spectra and PL spectra during laser irradiation, as show in Fig. 2(d), further supports that the PL is originating from the spontaneous emission from the radiative recombination of hot carriers, and the plasmonic mode enhances this spontaneous emission.

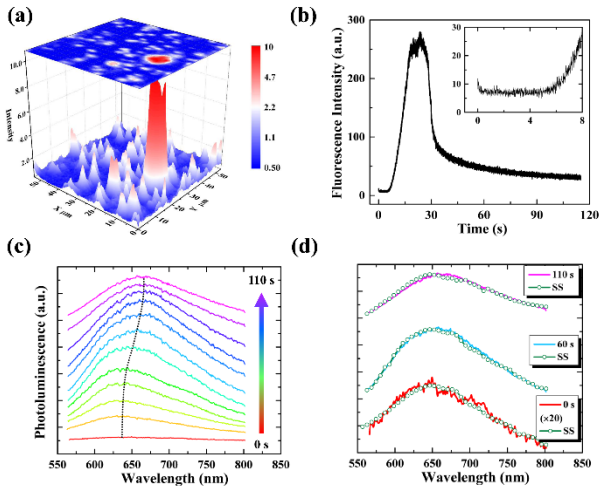

Fig. 2. PL enhancement and corresponding spectra profiles during laser irradiation. (a) Confocal PL imaging of the prepared sample. (b) Typical PL trajectory of aggregated NS-160 Au NSs during 405 nm laser irradiation at the power density of 6 MW/cm^2. (c) The corresponding spectral profiles under different irradiation duration. The integration is 1 s and time interval is 10 s. (d) PL and scattering spectra (SS) of aggregated NS-160 Au NSs after irradiation with duration of 0 s, 60 s and 110 s, respectively.

To verify that laser-induced PL enhancement are indicative of the whole sample, and also to analyze the influences on PL enhancement, the systematic experiments were carried out by varying: (i) the power density of 405 nm laser (irradiation on NS-160 with 0.3 MW/cm^2, 6 MW/cm^2, and 30 MW/cm^2, respectively); (ii) the wavelength of irradiation lasers (irradiation on NS-160 by 405 nm, 488 nm, and 532 nm CW laser at the power density of 6 MW/cm^2),

Optics EXPRESS

and (iii) the size of NSs (NS-60, NS-100, and NS-160 by 405 nm CW laser at the power density of 6 MW/cm^2). The results have been presented in Fig. 3 and 4, respectively. Here, two feature parameters are used to characterize the enhancement effects: the enhancement factor, *EF*, and the maximum enhancement time, T_m (the time reaching the maximum PL intensity from the beginning). *EF* expresses the enhancement effect, while T_m denotes the dynamics of the enhancement process.

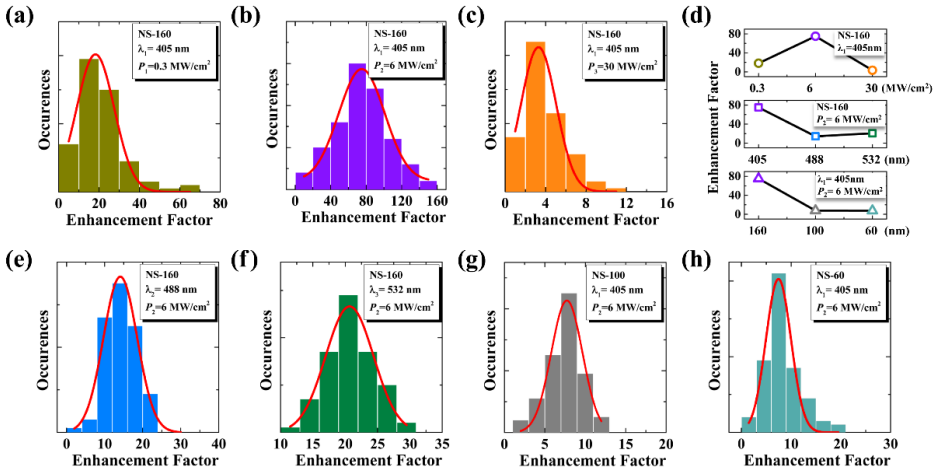

Fig. 3. PL enhancement factors vary under different irradiation conditions. (a)-(c) Different power density, 0.3 MW/cm^2, 6 MW/cm^2, and 30 MW/cm^2, respectively. (b), (e), and (f) Different laser wavelength, 405 nm, 488 nm, and 532 nm, respectively. (b), (g), and (h) Different averaged diameter, NS-160, NS-100, and NS-60, respectively. (d) Summarized central values of histograms under different conditions.

Figure 3 presents the variations of *EF* under different conditions. Note that the histograms of *EF* emerge broader distributions. The reasons behind this phenomenon may be divided into two categories: the heterogeneity of the shape, and the varied distances among NSs (which will be discussed later). Here all the distributions were fitted by Gauss function and the central values were used as the indicator. As shown in Figs. 3(a)-3(c), when NSs and laser wavelength were maintained at Ns-160 and 405 nm, their *EF* have dramatic change. As the power density increases from 0.3 MW/cm^2 to 6 MW/cm^2, *EF* increases from 18.2 to 75.0. However, *EF* plummets to 3.3, as the power density reaches to 30 MW/cm^2. This result reveals that the power density is a significant parameter regarding laser-induced PL enhancement. On the other hand, when maintaining the power density at 6 MW/cm^2 but varying the wavelength, *EF* decreases from 75.0 for 405 nm to 14.1 for 488 nm, and to 20.7 for 532 nm, respectively. Comparing with the giant enhancement under 405 nm irradiation, we can found that PL enhancement under 488 nm and 532 nm are moderate. These results are also appropriate for NSs with smaller diameters, as shown in Fig. 11. On the other side, comparing with NS-160, those of NS-100 and NS-60 under the same irradiation condition are moderate as well, as illustrated in Figs. 3(g) and 3(h), where the *EF* is 7.7 for NS-100, and 7.5 for NS-60, respectively. The variations of *EF* under different conditions have also been summarized in Fig. 3(d). Hence, this series of experiments shows that laser-induced PL enhancement are much more pronounced for Au NSs with larger diameter.

The analysis of corresponding enhancement times, T_m, used to reveal the dynamics of enhancement process, have been presented in Fig. 4. Similar with *EF*, T_m also varies vastly as the irradiation conditions change. Under the power density of 0.3 MW/cm^2, the time reaching the maximum PL is up to 107.1 s, while it rapidly decreases to 4.4 s as the power density increases to 6 MW/cm^2, as illustrated in Figs. 4(a) and 4(b). However, as the power density increases to 30 MW/cm^2, the whole PL enhancement and quenching process are completed in

Optics EXPRESS

one second for most cases (as illustrated in Fig. 13). Thus, as presented in Fig. 4(c), its histogram emerges a non-Gauss distribution, with the maximum value equaling to 0.25 s. On the other aspect, when maintaining the power density, T_m for 405 nm, 488 nm, and 532 nm are 4.4s, 5.0 s, and 24.3 s, respectively. The result indicates that the enhanced dynamics under 405 nm and 488 nm are similar, while 532 nm is different. It may be explored by the excitation spectrum of NS-160, as illustrated in Fig. 1(e). Both 405 nm and 488 nm are situated at the electronic transition from 5*d* to 6*sp* bands [21,34], while 532 nm is situated at the quadrupolar plamon mode of NS-160. Au NSs interacts with shorter wavelength may lose more energy to the phonon lattice and thus enhance the photothermal effect. This conclusion can be further supported by the PL enhancement of NS-100 and NS-60 under laser irradiation with three wavelengths, as shown in Fig. 12. Additionally, no significant difference of T_m are observed on the Au NSs with different diameters, as shown in Figs. 4(b), 4(g) and 4(h). The variations of T_m under different conditions have also been summarized in Fig. 4(d).

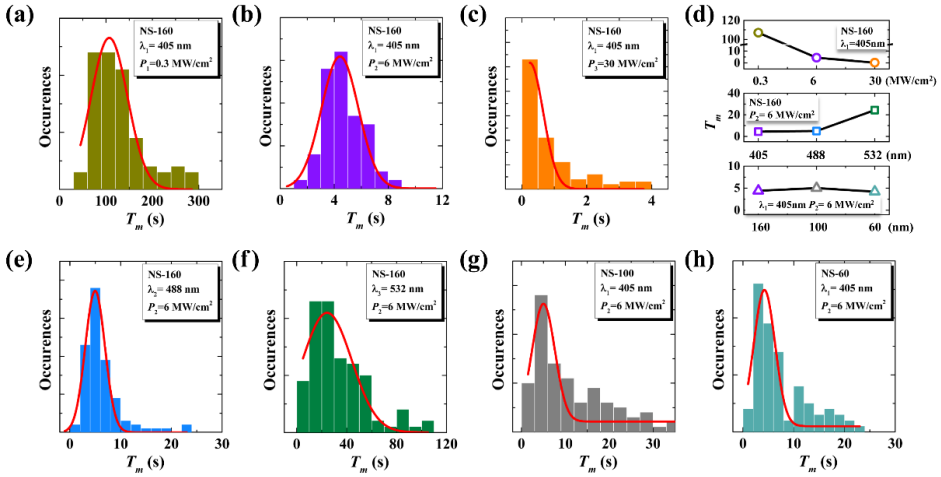

Fig. 4. Maximum enhancement times vary under different irradiation conditions. (a)-(c) Different power density, 0.3 MW/cm^2, 6 MW/cm^2, and 30 MW/cm^2, respectively. (b), (e), and (f) Different laser wavelength, 405 nm, 488 nm, and 532 nm, respectively. (b), (g), and (h) Different averaged diameter, NS-160, NS-100, and NS-60, respectively. (d) Summarized central values of histograms under different conditions.

Here we suggest that the experimental results are originating from the laser-induced photothermal welding and reshaping of adjacent Au NSs. Many previous works have reported the melting, reshaping and fragmentation of Au nanoparticles in aqueous by pulsed laser irradiation [34–36]. Baumberg group has demonstrated laser threading of Au nanoparticles string by using unfocussed femtosecond laser with averaged power density of 90 MW/cm^2 [37]. Guillermo and associates designed the tip-to-tip assembly and welding of Au nanorods by irradiation with femtosecond laser pulses [38]. Not merely the pulsed laser but also the CW laser and even non-coherent light can be used to reshape and/or weld nanostructures. The decrease in the length and increase in the width of Au nanorods after irradiation with 808 nm CW laser have been clearly determined by David *et al* [28]. On the other hand, the welding of silver nanowires have been achieve by the irradiation of both 532 nm CW laser and broadband tungsten-halogen lamp [39,40]. On the basis of these previous works, we propose that the tightly focused CW laser with high power density (in MW/cm^2) will melt the surface of Au NSs, and weld the adjust NSs. The dramatically enhanced light field in the crevices around the welding areas result in the giant PL enhancement. Further laser irradiation will reshape the welded Au NSs and give rise to the variation in the spectral profiles. The mechanisms expected are drawn schematically in Fig. 5 and are discussed below:

Optics EXPRESS

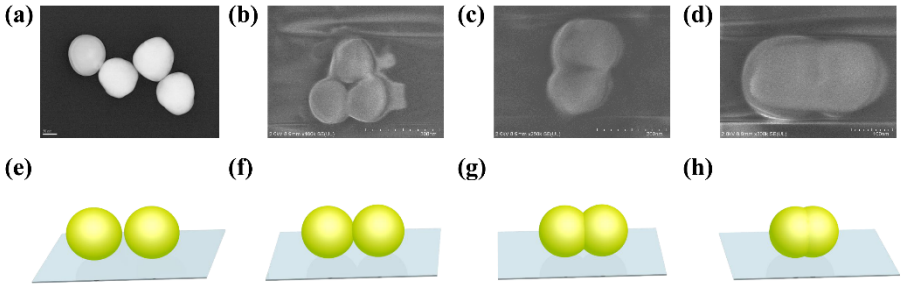

Fig. 5. Proposed PL enhancement mechanism. (a)TEM image of prepared NS-160, (b)-(d) SEM images of NS-160 observed after different irradiation duration. (e-h) Representation welding and reshaping of Au NSs during laser irradiation.

(i) To concisely illustrate the welding and reshaping of Au NSs, SEM images of dimer or trimer NS-160 observed after different irradiation duration have been presented in Figs. 5(b)-5(d). (The SEM images of intensively aggregated NSs have been presented in Fig. 14) The corresponding schematic represented by a pair of imperfect NSs have been shown in Figs. 5(e)-5(h). As we mentioned above, the areas where PL can be enhanced during laser irradiation always emerges stronger PL intensity at the initial. We have attributed the phenomenon to the aggregation of Au NSs, as shown in Figs. 5(a) and 5(e). According to the previous works, the aggregated NSs will enhance the local light field intensively as well [19,20,38]. Thus, the plasmonic near-field enhancement in the surrounding of original Au NSs is another contribution to the PL enhancement.

(ii) When the laser is focused on Au NSs for a short duration, photothermal effect will melt the surface and modify the shape of NSs, which may lead the formation of welding areas between the adjacent NSs, as illustrated in Fig. 5(b). The sharp contact point or the crevices [37] (Fig. 5(f)) around the welding areas will present extremely strong light field. Thus, PL from NSs can be dramatically enhanced. In the case, the time reaching the maximum PL intensity is decided by the formation of sharpest contacts or crevices. When the power density of irradiation laser is low, it takes a long time to form the welding areas, thus T_m is up to 107.1 s under 0.3 MW/cm^2, as presented in Fig. 4(a). On the other hand, in view of the slow process, the welding areas must be relative smooth, therefore the enhancement effect are moderate, as presented in Fig. 3(a). In contrast, when the power density is appropriate, the welding areas will be formed in a short, as 4.4 s shown in Fig. 4(b). Meanwhile the rapid process will lead the welding areas roughly or give rise to many crevices, which will result in dramatically enhanced local light field and thus giant PL enhancement, as given in Fig. 3(b). However, when the power density is too high, the formation of welding areas and further reshaping will be completed in a very short duration (sub-second or even shorter). As a consequent, the enhanced process is rather short and hard to observe, as illustrated in Figs. 3(c) and 4(c), respectively.

(iii) After the formation of welding areas, the jointed Au NSs will be reshaped by further laser irradiation. During this stage, the aggregated Au NSs will form different shape, as shown in Fig. 5 and Fig. 14. On the other side, even though the roughness or crevices will be eliminated gradually, resulting in the quenching of PL, there are some sharp areas still maintaining. The local field enhancement is still stronger than the original NSs. As a consequent, PL during the slow decay stage remains stronger than the initial value, as presented in Fig. 2(b).

(iv) At last, the new formed Au nanoparticles will be further melted and reshaped by laser irradiation, as illustrated in Figs. 5(d) and 5(h). During this stage, the field enhancement will be weakened persistently but slowly, resulting in the slow decay shown in Fig. 2(b).

Optics EXPRESS

On the basis of the proposed mechanism, the moderate PL enhancement of NS-100 and NS-60 (Figs. 3(g) and 3(h)) is reasonable. Due to the faceted rather than smooth edges of smaller NSs, the local field enhancement of the original NSs is already strong. Thus, the further field enhancement arising from the welding areas are not so pronounced. Although, the giant PL enhancement for the large diameter NSs is achieved undoubtedly. This study will develop biotechnological applications of Au nanoparticles, especially PL labelling and imaging by CW laser, beyond TPPL by femtosecond laser [19,20]. In particular, PL imaging with CW laser is more competitive, due to less expensive, smaller, more portable and clinically compatible than pulsed counterparts [28]. To show the potential application in Au-based PL imaging after enhancement, we investigate the stability of enhanced PL under normally laser irradiation, as illustrated in Fig. 6. The 405 nm CW laser with power density of 6 MW/cm^2 and 0.12 MW/cm^2 is alternating to irradiate the Au NSs, and collect their PL. In the first 5 s under high power density, PL is enhanced from 7.5 thousand counts per second (kcps) to 74.3 kcps. In the next 5 s, the laser was altered to low power density. Although the PL is weaker, only conventional fluctuation rather than enhancement or decay can be found during this stage. On the other word, the enhanced PL from Au NSs is very stable under normal laser irradiation (generally used in photothermal therapy or drug delivery). The stability of PL under different stages of enhanced process further support this conclusion.

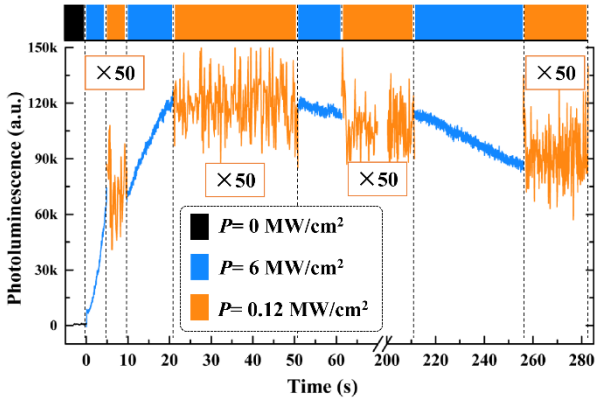

Fig. 6. PL trajectory of NS-160 under 405 nm laser irradiation with different power density. For convenience of comparison, PL intensity under 0.12 MW/cm^2 were multiplied by 50.

We also should keep in mind that the enhancement mechanism is not fully understood so far, such as the wavelength-dependent results. Therefore, the investigations of PL enhancement under laser wavelengths resonance with dipolar plasmon mode and that far away from the resonance (such as infrared laser) might be able to yield a further understanding. On the other hand, the combination of laser irradiation and *in suit* electron tomography experiments is also vital for uncovering the laser-induced welding process. These attempts will provide a controlled fashion to build up functionalized plasmonic nanostructures, which are hard to access reliably by top-down fabrication or bottom-up approaches. This kind of control over nanostructures' morphology by CW laser irradiation might be further applied in the scalable fabrication of electronic and optoelectronics [38].

4. Conclusions

In summary, we have presented that the CW laser irradiation is a powerful tool to weld the adjacent Au NSs and dramatically enhance their PL. The systematic experimental results reveal that the PL enhancement is influenced by the power density and wavelength of irradiation laser, as well as the size of NSs. Among them, the NS-160 emerges more than two orders of magnitude PL enhancement, under the irradiation of 405 nm CW laser at the power density of 6 MW/cm^2. In the case, the maximum PL enhancement can be achieved only in

Optics EXPRESS

several seconds. We attributed the giant PL enhancement to laser-induced welding and reshaping of adjacent Au NSs, which will dramatically enhance the incidence light field in the crevices around the welding areas and thus result in the PL enhancement. The proposed mechanism can explore observed phenomena reasonably good, including *EF* and T_m under different irradiation conditions as well as the variation of spectral profiles during laser irradiation. These results show promising applications of Au nanoparticles in the biological fields, such as PL labelling and imaging in clinical medicine. The welding of Au NSs by CW laser also emerges potential applications in the fabrication of functionalized plasmonic nanostructures' and related electronic and optoelectronic devices.

Appendix

To further support our conclusions, we supplied supplementary materials. Figure 7 presents the morphology characterizations of NS-100 and NS-160, to illustrate their size distributions. Figure 8 displays the PL spectra and the corresponding scattering spectra of Au NSs used in the experiment. The similarity of the two spectra further suggests that the PL of Au NSs can be attributed to the spontaneous emission from the radiative recombination of hot carriers. Figure 9 shows the SEM images of prepared samples, indicating the aggregation of Au NSs. Figure 10 gives the maximum *EF* observed in the experiment, of which the maximum PL intensity was more than 150 times stronger than the initial intensity. Figures 11 and 12 present the *EF* and T_m of NS-100 and NS-60 under irradiation with different wavelengths, indicating that the PL enhancement under 488 nm and 532 nm is smaller than that under 405 nm. To explore the PL enhancement and quenching process under different power densities, Figure 13 shows typical PL trajectories of NS-160 under power density of 0.3 MW/cm^2, 6MW/cm^2 and 30 MW/cm^2, respectively. Figure 14 present the SEM images of NS-160 after laser irradiation. The highlighted areas manifest the welding and reshaping of aggregated Au NSs during laser irradiation.

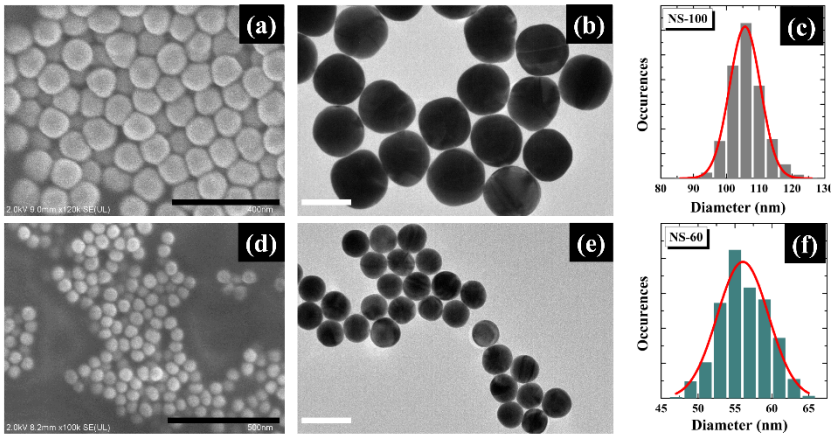

Fig. 7. Morphology characterization of Au NSs. (a) SEM and (b) TEM images of NS-100. Scale bar: (a) 400 nm, (b) 100 nm. (c) Size distribution of NS-100, fitted by Gauss function with central at 105 nm and FWHM of 10 nm. (d) SEM and (e) TEM images of NS-60. Scale bar: (d) 500 nm, (e) 100 nm. (f) Size distribution of NS-60, fitted by Gauss function with central at 56 nm and FWHM of 7 nm.

Optics EXPRESS

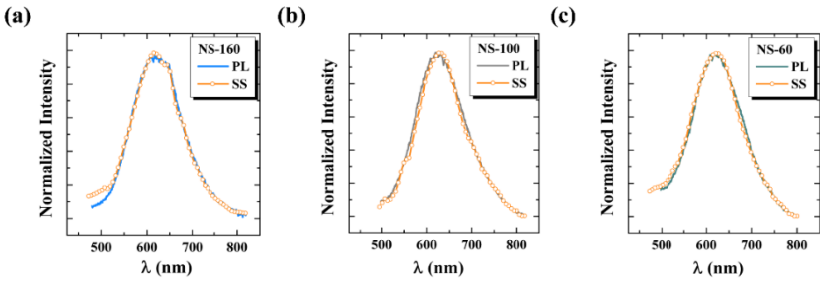

Fig. 8. PL spectra and the corresponding scattering spectra (SS) of NS-160 (a), NS-100 (b), and NS-60 (c), respectively.

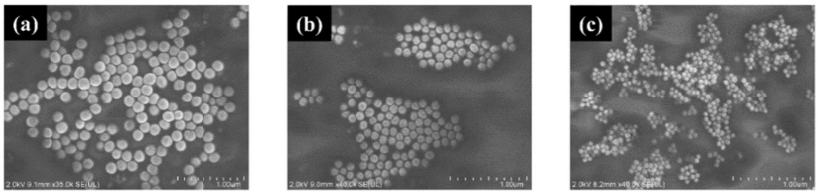

Fig. 9. SEM characterization of prepared samples. (a) NS-160. (b) NS-100. (c) NS-60.

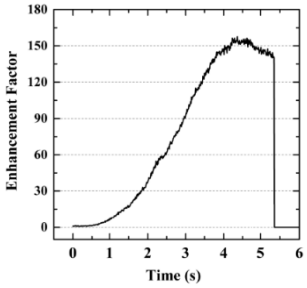

Fig. 10. Enhancement factor of NS-160 as a function of irradiation duration. The sample was irradiated by 405 nm at the power density of 6 MW/cm^2. The PL enhancement factor is up to 150.

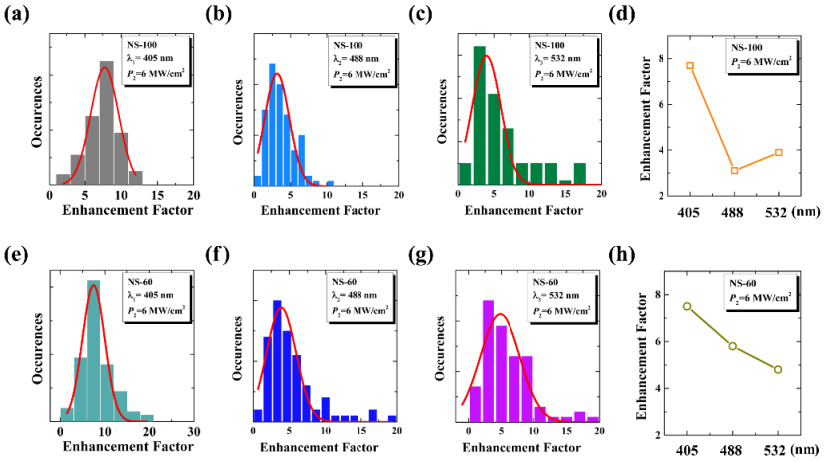

Fig. 11. PL enhancement factors of NS-100 and NS-60 under different laser wavelength with the power density of 6 MW/cm^2. (a)-(c) NS-100 under 405 nm, 488 nm, and 532 nm, respectively. (e)-(g) NS-60 under 405 nm, 488 nm, and 532 nm, respectively. (d) and (h) Summarized enhancement under different wavelengths.

Optics EXPRESS

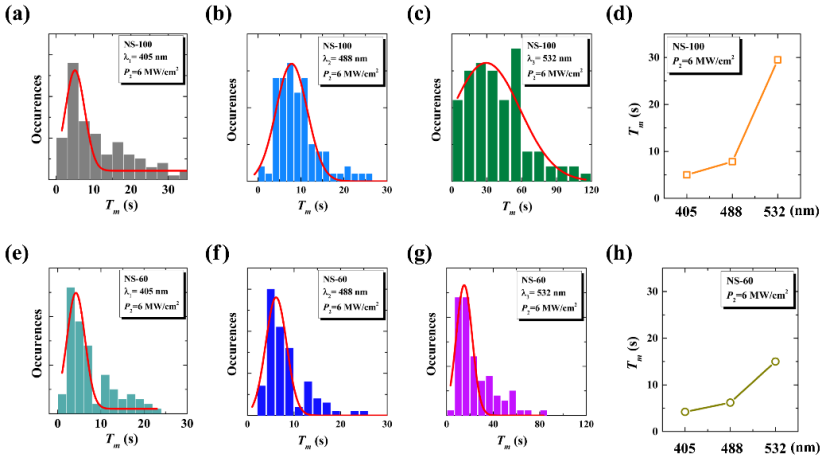

Fig. 12. Maximum enhancement times of NS-100 and NS-60 under different laser wavelength with the power density of 6 MW/cm2. (a)-(c) NS-100 under 405 nm, 488 nm, and 532 nm, respectively. (e)-(g) NS-60 under 405 nm, 488 nm, and 532 nm, respectively. (d) and (h) Summarized enhancement times under different wavelengths.

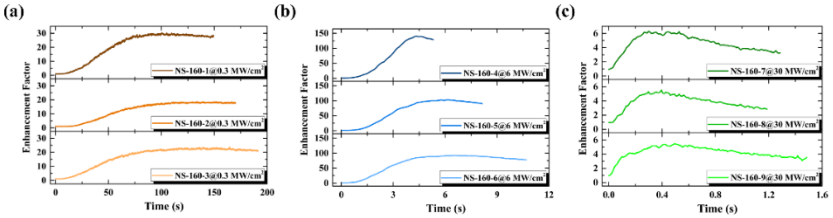

Fig. 13. Typical enhancement factor of NS-160 under power density of (a) 0.3 MW/cm^2, (b) 6 MW/cm^2, and (c) 30 MW/cm^2, respectively.

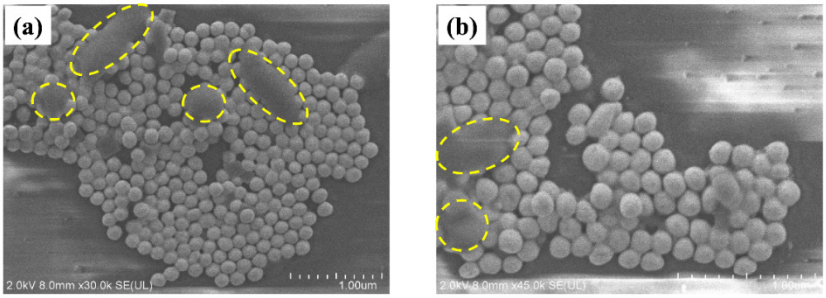

Fig. 14. SEM images of NS-160 observed after laser irradiation. The melt Au NSs have been highlighted by dashed lines.

Funding

National Key Research and Development Program of China (2017YFA0304203), National Natural Science Foundation of China (11434007), Natural Science Foundation of China (NSFC) (61875109, 61527824, 61675119, 11504216, and 61605104), PCSIRT (IRT_17R70), 1331KSC and 111 project (D18001).

References

1. H. A. Atwater and A. Polman, “Plasmonics for improved photovoltaic devices,” Nat. Mater. **9**(3), 205–213 (2010).
2. G. Baffou and R. Quidant, “Nanoplasmonics for chemistry,” Chem. Soc. Rev. **43**(11), 3898–3907 (2014).

Optics EXPRESS

3. D. K. Gramotnev and S. I. Bozhevolnyi, "Nanofocusing of electromagnetic radiation," Nat. Photonics **8**(1), 13–22 (2014).
4. L. Liu, S. Ouyang, and J. Ye, "Gold-nanorod-photosensitized titanium dioxide with wide-range visible-light harvesting based on localized surface plasmon resonance," Angew. Chem. Int. Ed. Engl. **52**(26), 6689–6693 (2013).
5. W. Hou and S. B. Cronin, "A Review of Surface Plasmon Resonance-Enhanced Photocatalysis," Adv. Funct. Mater. **23**(13), 1612–1619 (2013).
6. K. M. Mayer and J. H. Hafner, "Localized surface plasmon resonance sensors," Chem. Rev. **111**(6), 3828–3857 (2011).
7. M. Kauranen and A. V. Zayats, "Nonlinear plasmonics," Nat. Photonics **6**(11), 737–748 (2012).
8. A. M. Fales, W. C. Vogt, T. J. Pfefer, and I. K. Ilev, "Quantitative Evaluation of Nanosecond Pulsed Laser-Induced Photomodification of Plasmonic Gold Nanoparticles," Sci. Rep. **7**(1), 15704 (2017).
9. V. Juvé, M. F. Cardinal, A. Lombardi, A. Crut, P. Maioli, J. Pérez-Juste, L. M. Liz-Marzán, N. Del Fatti, and F. Vallée, "Size-dependent surface plasmon resonance broadening in nonspherical nanoparticles: single gold nanorods," Nano Lett. **13**(5), 2234–2240 (2013).
10. M. M. Miller and A. A. Lazarides, "Sensitivity of metal nanoparticle surface plasmon resonance to the dielectric environment," J. Phys. Chem. B **109**(46), 21556–21565 (2005).
11. S. K. Ghosh and T. Pal, "Interparticle coupling effect on the surface plasmon resonance of gold nanoparticles: from theory to applications," Chem. Rev. **107**(11), 4797–4862 (2007).
12. J. Mertens, M. E. Kleemann, R. Chikkaraddy, P. Narang, and J. J. Baumberg, "How Light Is Emitted by Plasmonic Metals," Nano Lett. **17**(4), 2568–2574 (2017).
13. L. Tong, T. Zhu, and Z. Liu, "Approaching the electromagnetic mechanism of surface-enhanced Raman scattering: from self-assembled arrays to individual gold nanoparticles," Chem. Soc. Rev. **40**(3), 1296–1304 (2011).
14. C. Jiang, T. Zhao, P. Yuan, N. Gao, Y. Pan, Z. Guan, N. Zhou, and Q. H. Xu, "Two-photon induced photoluminescence and singlet oxygen generation from aggregated gold nanoparticles," ACS Appl. Mater. Interfaces **5**(11), 4972–4977 (2013).
15. A. Slablab, L. Le Xuan, M. Zielinski, Y. de Wilde, V. Jacques, D. Chauvat, and J. F. Roch, "Second-harmonic generation from coupled plasmon modes in a single dimer of gold nanospheres," Opt. Express **20**(1), 220–227 (2012).
16. A. Camposeo, L. Persano, R. Manco, Y. Wang, P. Del Carro, C. Zhang, Z.-Y. Li, D. Pisignano, and Y. Xia, "Metal-Enhanced Near-Infrared Fluorescence by Micropatterned Gold Nanocages," ACS Nano **9**(10), 10047–10054 (2015).
17. H. He, C. Xie, and J. Ren, "Nonbleaching fluorescence of gold nanoparticles and its applications in cancer cell imaging," Anal. Chem. **80**(15), 5951–5957 (2008).
18. R. A. Sperling, P. Rivera Gil, F. Zhang, M. Zanella, and W. J. Parak, "Biological applications of gold nanoparticles," Chem. Soc. Rev. **37**(9), 1896–1908 (2008).
19. Z. Guan, N. Gao, X. F. Jiang, P. Yuan, F. Han, and Q. H. Xu, "Huge enhancement in two-photon photoluminescence of Au nanoparticle clusters revealed by single-particle spectroscopy," J. Am. Chem. Soc. **135**(19), 7272–7277 (2013).
20. F. Han, Z. Guan, T. S. Tan, and Q. H. Xu, "Size-dependent two-photon excitation photoluminescence enhancement in coupled noble-metal nanoparticles," ACS Appl. Mater. Interfaces **4**(9), 4746–4751 (2012).
21. E. Dulkeith, T. Niedereichholz, T. Klar, J. Feldmann, G. von Plessen, D. Gittins, K. Mayya, and F. Caruso, "Plasmon emission in photoexcited gold nanoparticles," Phys. Rev. B Condens. Matter Mater. Phys. **70**(20), 205424 (2004).
22. A. Gaiduk, M. Yorulmaz, and M. Orrit, "Correlated absorption and photoluminescence of single gold nanoparticles," ChemPhysChem **12**(8), 1536–1541 (2011).
23. Q. Wang, G. Lu, L. Hou, T. Zhang, C. Luo, H. Yang, G. Barbillon, F. H. Lei, C. A. Marquette, P. Perriat, O. Tillement, S. Roux, Q. Ouyang, and Q. Gong, "Fluorescence correlation spectroscopy near individual gold nanoparticle," Chem. Phys. Lett. **503**(4-6), 256–261 (2011).
24. M. Yorulmaz, S. Khatua, P. Zijlstra, A. Gaiduk, and M. Orrit, "Luminescence quantum yield of single gold nanorods," Nano Lett. **12**(8), 4385–4391 (2012).
25. D. Pissuwan, T. Niidome, and M. B. Cortie, "The forthcoming applications of gold nanoparticles in drug and gene delivery systems," J. Control. Release **149**(1), 65–71 (2011).
26. W. I. Choi, J.-Y. Kim, C. Kang, C. C. Byeon, Y. H. Kim, and G. Tae, "Tumor Regression In Vivo by Photothermal Therapy Based on Gold-Nanorod-Loaded, Functional Nanocarriers," ACS Nano **5**(3), 1995–2003 (2011).
27. M.-F. Tsai, S.-H. G. Chang, F.-Y. Cheng, V. Shanmugam, Y.-S. Cheng, C.-H. Su, and C.-S. Yeh, "Au Nanorod Design as Light-Absorber in the First and Second Biological Near-Infrared Windows for in Vivo Photothermal Therapy," ACS Nano **7**(6), 5330–5342 (2013).
28. D. Harris-Birtill, M. Singh, Y. Zhou, A. Shah, P. Ruenraroengsak, M. E. Gallina, G. B. Hanna, A. E. G. Cass, A. E. Porter, J. Bamber, and D. S. Elson, "Gold nanorod reshaping in vitro and in vivo using a continuous wave laser," PLoS One **12**(10), e0185990 (2017).
29. Q. Ruan, L. Shao, Y. Shu, J. Wang, and H. Wu, "Growth of Monodisperse Gold Nanospheres with Diameters from 20 nm to 220 nm and Their Core/Satellite Nanostructures," Adv. Opt. Mater. **2**(1), 65–73 (2014).

Optics EXPRESS

30. H. T. Zhou, C. B. Qin, R. Y. Chen, G. F. Zhang, L. T. Xiao, and S. T. Jia, "Electric field induced fluorescence hysteresis of single molecules in poly(methyl methacrylate)," Appl. Phys. Lett. **105**(15), 153301 (2014).
31. Y. Gao, C. Qin, Z. Qiao, B. Wang, W. Li, G. Zhang, R. Chen, L. Xiao, and S. Jia, "Imaging and spectrum of monolayer graphene oxide in external electric field," Carbon **93**, 843–850 (2015).
32. Y. Y. Cai, J. G. Liu, L. J. Tauzin, D. Huang, E. Sung, H. Zhang, A. Joplin, W. S. Chang, P. Nordlander, and S. Link, "Photoluminescence of Gold Nanorods: Purcell Effect Enhanced Emission from Hot Carriers," ACS Nano **12**(2), 976–985 (2018).
33. Y. Fang, W. S. Chang, B. Willingham, P. Swanglap, S. Dominguez-Medina, and S. Link, "Plasmon Emission Quantum Yield of Single Gold Nanorods as a Function of Aspect Ratio," ACS Nano **6**(8), 7177–7184 (2012).
34. S. V. Makarov, A. S. Zalogina, M. Tajik, D. A. Zuev, M. V. Rybin, A. A. Kuchmizhak, S. Juodkazis, and Y. Kivshar, "Light-Induced Tuning and Reconfiguration of Nanophotonic Structures," Laser Photonics Rev. **11**(5), 1700108 (2017).
35. D. Zhang, B. Gökce, and S. Barcikowski, "Laser Synthesis and Processing of Colloids: Fundamentals and Applications," Chem. Rev. **117**(5), 3990–4103 (2017).
36. S. Hashimoto, D. Werner, and T. Uwada, "Studies on the interaction of pulsed lasers with plasmonic gold nanoparticles toward light manipulation, heat management, and nanofabrication," J. Photochem. Photobiol. Chem. **13**(1), 28–54 (2012).
37. L. O. Herrmann, V. K. Valev, C. Tserkezis, J. S. Barnard, S. Kasera, O. A. Scherman, J. Aizpurua, and J. J. Baumberg, "Threading plasmonic nanoparticle strings with light," Nat. Commun. **5**(1), 4568 (2014).
38. G. González-Rubio, J. González-Izquierdo, L. Bañares, G. Tardajos, A. Rivera, T. Altantzis, S. Bals, O. Peña-Rodríguez, A. Guerrero-Martínez, and L. M. Liz-Marzán, "Femtosecond Laser-Controlled Tip-to-Tip Assembly and Welding of Gold Nanorods," Nano Lett. **15**(12), 8282–8288 (2015).
39. S. W. Dai, Q. Li, G. P. Liu, H. B. Yang, Y. Q. Yang, D. Zhao, W. Wang, and M. Qiu, "Laser-induced single point nanowelding of silver nanowires," Appl. Phys. Lett. **108**(12), 121103 (2016).
40. E. C. Garnett, W. Cai, J. J. Cha, F. Mahmood, S. T. Connor, M. Greyson Christoforo, Y. Cui, M. D. McGehee, and M. L. Brongersma, "Self-limited plasmonic welding of silver nanowire junctions," Nat. Mater. **11**(3), 241–249 (2012).